ACCSCIENCE PUBLISHING

Advances in Radiotherapy & Nuclear Medicine

ORIGINAL RESEARCH ARTICLE

Design, characterization, and fabrication of a 3D-printed patient-specific and personalized cranial immobilization system for radiotherapy treatment

NourElHouda Touil[1], Karim Benkahila[2], and Faycal Kharfi[1]*

[1]Department of Physics, Faculty of Sciences, University Sétif1-Ferhat Abbas, Sétif, Algeria

[2]Department of Radiotherapy, Fighting against Cancer Medical Centre of Sétif, Sétif, Algeria

Abstract

Accurate immobilization is essential in cranial radiotherapy because modern treatment techniques rely on high geometric precision and tight setup tolerances. Conventional thermoplastic masks remain the clinical standard, but they may be uncomfortable, anxiety-provoking, and insufficiently adapted to individual facial anatomy. This study investigates the design, fabrication, and preclinical validation of a personalized immobilization system composed of a facial shell and fixation belts. The necessary facial surface was acquired using an EinScan Pro+ scanner. The facial shell was designed in Meshmixer, while the fixation belts and hooks were modeled in Fusion 360 according to the geometry of a Klarity Optek™ indexing board. Final components were sliced in Cura and fabricated on an Artillery Sidewinder X1 printer. Polylactic acid (PLA) and thermoplastic polyurethane (TPU) were numerically evaluated in COMSOL Multiphysics 6.3 for thermal phase transition during printing, irradiation-induced heating under a 6 MV radiotherapy photon beam (400 MU/min for 15 min), and tensile mechanical behavior of the fixation belts. The workflow successfully produced a 2.5-mm-thick patient-specific immobilization device with excellent anatomical conformity and compatibility with the clinical support system. Simulated peak temperatures remained low for both PLA (27.85 °C) and TPU (28.45 °C), indicating thermal stability during photon irradiation. Mechanical simulations showed peak stress of approximately 0.7 MPa and maximum displacement (deformation) of 0.012 mm for PLA and 0.4 mm for TPU, both below a 1-mm tolerance threshold. The proposed workflow supports the feasibility of personalized 3D-printed cranial immobilization devices, with TPU emerging as a promising material because it combines structural stability with greater flexibility and patient comfort.

Keywords: Radiotherapy; Cranial immobilization; Personalized medicine; 3D printing; Structured-light scanning; Patient-specific device; COMSOL Multiphysics simulation

***Corresponding author:**
Faycal Kharfi
(kharfifaycl@univ-setif.dz)

Citation: Touil N, Benkahila K, Kharfi F. Design, characterization, and fabrication of a 3D-printed patient-specific and personalized cranial immobilization system for radiotherapy treatment. *Adv Radiother Nucl Med.* 2026;4(3):026270031. doi: 10.36922/ARNM026270031

Received: July 4, 2026

Revised: September 6, 2026

Accepted: September 11, 2026

Published online: September 23, 2026

Copyright: © 2026 Author(s). This is an Open-Access article distributed under the terms of the Creative Commons Attribution License, permitting distribution, and reproduction in any medium, provided the original work is properly cited.

Publisher's Note: AccScience Publishing remains neutral with regard to jurisdictional claims in published maps and institutional affiliations.

1. Introduction

Radiotherapy is built on a simple but unforgiving principle: the prescribed dose must reach the target repeatedly and precisely, while nearby healthy structures must be spared. In cranial radiotherapy, this requirement becomes even more demanding because the

treatment field often lies close to critical organs and late-responding normal tissues. As radiotherapy has evolved toward intensity-modulated radiotherapy, volumetric-modulated arc therapy, stereotactic treatments, and image-guided workflows, setup reproducibility has become inseparable from treatment quality.[1-5] A well-optimized treatment plan can lose part of its clinical value if patient positioning is not equally reproducible at the time of delivery.

Head immobilization devices are therefore a core part of cranial radiotherapy practice. Thermoplastic masks remain the most widely used solution because they are relatively simple, available in most departments, and compatible with routine workflows. However, they are not without limitations. In practice, standard thermoplastic masks may generate pressure points, claustrophobia, discomfort during repeated fractions, and imperfect conformity to subtle patient-specific facial anatomy. In some cases, anatomical changes over the course of treatment may also reduce fit quality. These issues are not merely ergonomic; they affect reproducibility, patient tolerance, and potentially the margins required around the target.[6-10]

Three-dimensional (3D) technologies offer a credible alternative. Structured-light scanning can capture facial anatomy without ionizing radiation, physical molding, or contact with the patient's skin. The resulting digital surface can then be translated into a personalized immobilization device using additive manufacturing. Over the past decade, 3D printing has expanded from a prototyping tool to a clinically relevant technology in oncology, radiotherapy, and biomedical engineering. It has been used for patient-specific boluses, compensators, phantoms, oral stents, anatomical models, surgical planning, and individualized accessories.[11-18] In the context of immobilization, 3D printing is attractive because it allows geometry to be tailored to the patient rather than forcing the patient to adapt to a generic shell.[19-23]

The present study was designed around that idea. It aims to create a patient-specific cranial immobilization device using a digital workflow that links structured-light surface acquisition, mesh post-processing, computer-aided design (CAD), fused deposition modeling (FDM) 3D printing,[24] and preclinical validation using multiphysics simulation. The work focused deliberately on workflow robustness, because a personalized device is only clinically relevant if the path from scanning to fabrication is technically coherent, reproducible, and safe.[25-36] In addition to the design and fabrication stages, the study examined the thermal and mechanical behavior of two candidate printing materials, polylactic acid (PLA) and thermoplastic polyurethane (TPU), under both printing-related and radiotherapy-related conditions. A practical fitting test on a clinical treatment support system was also performed to bridge the gap between digital design and real-world use.[37]

The underlying question was straightforward: can a personalized, 3D-printed cranial immobilization device be produced using accessible hardware and software while maintaining the geometric, thermal, and mechanical stability expected in radiotherapy? The results suggest a promising answer.

2. Materials and methods

2.1. Study design

This study developed a complete digital workflow for the fabrication and preclinical validation of a personalized head immobilization device for cranial radiotherapy.[25,29,35,36] The workflow included the following sequential stages:

(i) Acquisition of patient facial geometry using structured-light scanning
(ii) Digital post-processing of the 3D facial mesh
(iii) Design of the patient-specific facemask
(iv) Parametric design of the fixation belts and hooks
(v) Slicing and FDM fabrication
(vi) COMSOL Multiphysics numerical simulation
(vii) Real clinical fitting test on a radiotherapy support system

The final immobilization system was composed of two main elements: a patient-specific facial shell and lateral fixation belts with attachment hooks designed to lock onto a radiotherapy indexing board. In this work, two 3D printing materials were selected: TPU for the physical prototype because of its flexibility and anticipated patient-contact comfort, and PLA as a rigid comparative and alternative material if the application and receiving surface require it. The materials used are safe for the targeted radiotherapy clinical application and were studied in our previous work.[38]

2.2. Materials and equipment

2.2.1. Structured-light scanner

Facial geometry was acquired using the EinScan Pro+ handheld structured-light scanner (SHINING 3D, China), selected for its non-contact acquisition capability and suitability for high-resolution digitization of anatomical surfaces. The scanner supports handheld high-definition acquisition and is appropriate for medium-scale facial morphology capture.

2.2.2. 3D printer

Fabrication was performed using the Artillery Sidewinder X1 FDM printer (Shenzhen Yuntuchuangzhi Technology Co., Ltd., China), a large-format desktop system compatible with both rigid and flexible filaments. The printer was chosen because it combines a sufficient build volume with direct-drive extrusion, which is particularly advantageous for flexible materials such as TPU.

2.2.3. Clinical support system

The immobilization device was designed to be compatible with the Klarity Optek™ indexing board (Klarity Medical Products, LLC, United States of America [USA]), a carbon-fiber positioning support used for radiotherapy and computed tomography simulation. The board provides rigid, reproducible indexing while minimizing beam attenuation.

2.2.4. Printing materials

Two thermoplastic materials were considered:

- Polylactic acid as a rigid reference material for specific applications and the patient's receiving surface,
- Thermoplastic polyurethane as a flexible, patient-contact-oriented material.

Their thermal and mechanical properties were used as input parameters for COMSOL Multiphysics simulations (Table 1).

2.3. Workflow for generation of the patient-specific digital model

2.3.1. Structured-light surface acquisition

In this work, the required patient-specific model was created using structured-light scanning. The patient's facial surface was digitized using the Handheld HD Scan mode of the EinScan Pro+ scanner. The resolution of the light scanner used is 0.24 mm in fixed/automatic scan modes and ranges from 0.2 mm to 3.0 mm in handheld high-definition and rapid modes. A new project was created in the EinScan Pro environment (v3.1.0.2, SHINING 3D, China), and the acquisition settings were configured for high-detail anatomical capture.[19-23] The facial acquisition process is illustrated conceptually in Figure 1. The structured-light scanner projected a patterned light field onto the patient's face and reconstructed the external surface by analyzing pattern deformation over the anatomical contours. This approach allowed non-invasive capture of the forehead, brow ridges, zygomatic regions, nasal bridge, and periorbital contours.

The acquisition interface also allowed real-time monitoring of the point cloud during scanning, enabling operators to adjust brightness and capture stability. After completion of the acquisition stage, the software generated a dense 3D mesh comprising more than 4.9 million triangles, which served as the geometric basis for device design.

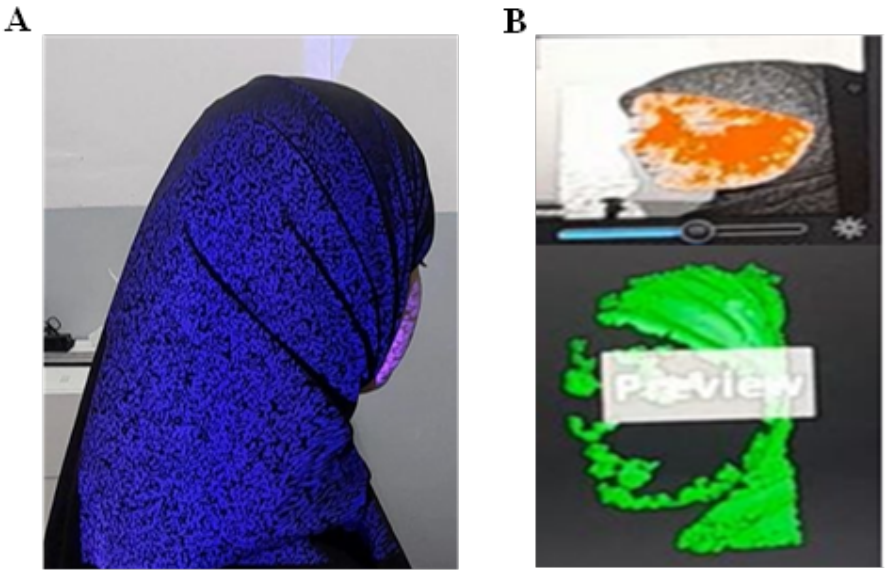

Figure 1. Structured-light acquisition workflow for the generation of the patient-specific facial model. Composite figure showing (A) structured-light projection and (B) preview stages corresponding to the EinScan Pro+ workflow.

Table 1. Physical, mechanical, and thermal properties used in the COMSOL Multiphysics simulations

Property	PLA	TPU
Density (ρ; g/cm^3)	1.24–1.26	1.15–1.25
Young's modulus (E; GPa)	3.0–3.5	0.01–0.1
Poisson's ratio (ν)	0.36	0.48–0.49
Tensile strength (MPa)	50–70	25–45
Glass transition temperature (Tg; K)	328–338	233–253
Melting temperature (K)	423–453	433–473
Thermal conductivity (k; W/m/K)	0.13–0.19	0.15–0.25
Specific heat capacity (C_p; J/kg/K)	1,200–1,800	1,500–2,000

Abbreviations: PLA: Polylactic acid; TPU: Thermoplastic polyurethane.

2.3.2. Post-processing of the facial mesh

The raw facial mesh underwent post-processing to improve usability for mask design. A sharpening filter was first applied to enhance anatomical contour definition, particularly around the nasal bridge and brow line. A smoothing filter was then used to reduce digital noise and surface irregularities, producing a cleaner and more homogeneous surface for subsequent shell generation.

This stage was important because a patient-specific mask is only as good as the surface it is derived from. Over-smoothed data may erase clinically useful contour information, whereas unfiltered data may reproduce scanning noise and compromise fit quality.

2.3.3. Design of the patient-specific immobilization device

(a) Design of the facial shell

The patient-specific facemask was designed in Autodesk Meshmixer (v.3.5.474, Autodesk, Inc., USA), which is well suited to surface-based manipulation of triangulated meshes. Using the processed facial surface as a template, a conformal shell was generated with a nominal thickness of 2.5 mm. The design included facial openings around the eyes, nose, and mouth to improve patient tolerance and facilitate breathing and visual comfort. Rather than forcing a generic geometry onto the face, the shell was offset directly from the patient's own surface, creating what may be described as a "second-skin" geometry adapted to the individual anatomy.

(b) Parametric design of fixation belts and hooks

The fixation subsystem was designed separately in Autodesk Fusion 360 (v.2606.1.36). The coordinates and dimensions of the fixation points on the Klarity Optek™ board were first measured, and these measurements were then used to build parametric fixation belts and attachment hooks. The decision to separate the anatomical shell from the fixation mechanics was deliberate. The facemask is anatomy-driven and therefore best handled with mesh-based design tools, whereas the belts and hooks depend on reproducible mechanical dimensions and are better suited to parametric CAD.

2.3.4. Slicing and 3D printing

The final STL files of the facial shell, belts, and hooks were imported into UltiMaker Cura (v.5.9.0, the Netherlands) for slicing and G-code generation. Printing preparation included orientation, layer-path generation, and definition of print parameters appropriate to the selected material. Fabrication was performed on the Artillery Sidewinder X1 using FDM. The layer resolution of the used printer ranges from 0.1 mm to 0.32 mm. In the physical prototype, TPU was selected as the principal manufacturing material because of its flexibility and expected patient-contact comfort. PLA was retained in the study as a comparative material for simulation-based characterization.[23]

2.4. COMSOL Multiphysics numerical characterization

To validate the structural and thermal behavior of the immobilization system before routine clinical use, multiphysics simulations were performed in COMSOL Multiphysics (v.6.3, COMSOL AB, Sweden). The simulation workflow integrated thermal and mechanical analyses for both PLA and TPU, as described in the following subsections.

2.4.1. Material properties

The input properties used in the simulations are summarized in Table 1. These included density, Young's modulus, Poisson's ratio, tensile strength, glass transition temperature, melting temperature, thermal conductivity, and specific heat capacity.

2.4.2. Phase-transition simulation during printing

The first simulation modeled the temperature-dependent phase transition of PLA and TPU during heating. The objective was to characterize how each material evolved from solid to molten state and to support the selection of suitable print temperatures.

COMSOL's Heat Transfer in Solids interface is based on conservation of energy, with conductive heat flux governed

by Fourier's law. For a stationary solid with no additional volumetric source, the basic equation reduces to:

$$\nabla.\left(k\nabla T\right)=0 \tag{1}$$

where T is the absolute temperature (K), and k is the thermal conductivity (W/m/K).

For a transient problem, the fundamental equation is:

$$\rho C_p \frac{\partial T}{\partial t}=\nabla.\left(k\nabla T\right)+Q \tag{2}$$

where ρ is the density (kg/m^3), Cp is the specific heat capacity (J/kg/K), and Q is the volumetric heat source (W/m^3).

With COMSOL's Phase Change Material formulation, the heat-capacity method was used. In this case, COMSOL does not need to explicitly track a moving solid/liquid interface. Instead, the phase transition occurs over a finite temperature interval ΔT.

The governing equation becomes:

$$\rho C_{p,app} \frac{\partial T}{\partial t}=\nabla.\left(k\nabla T\right)+Q \tag{3}$$

where the apparent heat capacity is:

$$C_{p,app}=C_P+C_L \tag{4}$$

and C_L represents the latent-heat contribution.

More generally,

$$C_{p,app}=C_{P,eq}+L\frac{d\alpha}{dT} \tag{5}$$

where L is the latent heat (J/kg), α is the phase fraction, and $d\alpha/dT$ is the distribution of phase transition over temperature.

COMSOL's Phase Change Material model specifically introduces latent heat through an apparent heat capacity rather than imposing an instantaneous temperature jump.

2.4.3. Simulation of photon irradiation–induced heating

The second simulation evaluated the thermal response of the printed materials under radiotherapy exposure. Indeed, a 6 MV radiotherapy photon beam delivered at 400 MU/min over 15 min was considered, corresponding to a total simulated irradiation time of 900 s. An incident radiation intensity of 23.809 W/m^2 was used in the simulation environment. The aim was to determine whether beam delivery could induce clinically meaningful heating, softening, or deformation of the immobilization device.

In this simulation, COMSOL Multiphysics used the model in **Equation 2,** with photon irradiation represented as an additional heat source. The following Fourier's law gives the conductive heat flux:

$$q=-k\nabla T \tag{6}$$

If the radiation is represented as an imposed surface heat flux, the boundary condition is given by:

$$-n.q=q_0=k\nabla T \tag{7}$$

where q_0 is the inward heat flux (23.809 W/m^2).

2.4.4. Mechanical simulation of fixation belts under clinical load

The third simulation assessed the tensile response of the fixation belts under traction and locking conditions representative of clinical use. Stress maps and maximum deformation (maximum total displacement) fields were calculated to evaluate the risk of mechanical failure and the magnitude of belt deformation under load. The main steps of this simulation are as follows:

(i) Step 1. Importation and definition of the belt geometry: The belt and hook geometry, designed parametrically in Fusion 360, is imported into COMSOL. The belt thickness, width, length, holes/fillets, and locking region are retained exactly as fabricated.
(ii) Step 2. Definition of the material: For each simulation, the corresponding material properties are assigned (Table 1). For a linear-elastic, isotropic approximation, the constitutive relation is given by:

$$\sigma=C/\varepsilon,\quad \varepsilon=\frac{1}{2}\left[\nabla u+\left(\nabla u\right)^T\right] \tag{8}$$

where u is the displacement vector; ε is the strain tensor, which describes the local deformation of the material; and C is the fourth-order elasticity (stiffness) tensor, which relates strain to stress and contains the material's elastic properties. For an isotropic material, C is determined by only two independent elastic constants, Young's modulus E and Poisson's ratio v. The constitutive equation can therefore be written more conveniently as:

$$\sigma=2G\varepsilon+\lambda t_r\left(\varepsilon\right)I \tag{9}$$

where G is the shear modulus given by:

$$G = \frac{E}{2(1+\upsilon)} \tag{10}$$

λ is the first Lamé parameter given by:

$$\lambda = \frac{E\nu}{(1+\nu)(1-2\nu)} \tag{11}$$

I is the second-order identity tensor (the tensor equivalent of the number 1).

Thus, the COMSOL model is described by: C ⟷ E,ν and ε ⟷ deformation produced by the applied belt load.

The resulting σ is then used to calculate the von Mises stress and the displacement field. Thus, COMSOL's Solid Mechanics formulation solves the mechanical equilibrium problem, and the implementation is based on the principle of virtual work, with stresses obtained from the constitutive relation.

(iii) Step 3. Application of the fixation constraint: The portion of the belt/hook that is physically constrained by the indexing system is assigned a fixed constraint (explicitly defined equivalent connector/contact condition). COMSOL stationary structural model requires sufficient constraints to eliminate rigid-body translations and rotations.

(iv) Step 4: Application of the traction/load: The opposite belt region is subjected to the traction representing the clinical tightening/pulling condition. A critical clinical stress scenario is considered by applying a uniform mechanical boundary load of 2 kPa across the internal contact surfaces of the belt. Simultaneously, the resulting total displacement magnitude across the entire geometry was analyzed to quantify the spatial rigidity of the components. Evaluating this sub-micrometric deflection profile is essential to verify that the mechanical deformation under pressure does not deviate from the strict millimeter-level spatial tolerances generally required in high-precision radiotherapy.

(v) Step 5. Solution of the stationary structural problem: COMSOL's Solid Mechanics interface solves the mechanical equilibrium equations together with a constitutive material law. For a quasi-static model, the fundamental equilibrium equation is:

$$\Delta\sigma + f = 0 \tag{12}$$

where σ is the Cauchy stress tensor and f is the body force per unit volume.

The study concerns slow manual/traction loading rather than dynamic impact, so a quasi-static structural analysis was used.

(vi) Step 6.- Calculating the stress field: After solving for u, COMSOL obtains the strain field and then the stress tensor. For the von Mises stress:

$$\sigma_{vM} = \sqrt{\frac{(\sigma_1-\sigma_2)^2+(\sigma_2-\sigma_3)^2+(\sigma_3-\sigma_1)^2}{2}} \tag{13}$$

where σ_1, σ_2, and σ_3 are the principal stresses.

The resulting spatial distribution is plotted as the von Mises stress map. In the present model, the maximum was concentrated at the locking hinge, which is mechanically reasonable because this is the principal load-transfer/constraint region ($\sigma_{vM,max} \approx 0.7$ MPa). For both considered materials, a useful quantitative safety indicator is given by:

$$SF_\sigma = \frac{\sigma_{allowed}}{\sigma_{vM,max}} \tag{14}$$

Using the lower ends of the tensile-strength ranges only as a conservative screening comparison:

- PLA: 50/0.7≈71
- TPU: 25/0.7≈36

(vii) Step 7. Calculation of the deformation field: The total displacement is obtained from the three displacement components by:

$$u_{tot} = \sqrt{u_x^2 + u_y^2 + u_z^2} \tag{15}$$

The maximum value over the belt domain is then:

$$u_{max} = \max(u_{tot}) \tag{16}$$

The effective values used in the performed simulation are ρ of 1,240 kg/m^3, an isotropic Young's modulus (E) of 3.6 GPa, and a Poisson's ratio (ν) of 0.35 for PLA, and ρ of 120 kg/m^3, an isotropic Young's modulus (E) of 0.1 GPa, and a Poisson's ratio (ν) of 0.48 for TPU.

2.5. Clinical fitting test

A practical fitting test of the fabricated immobilization device was performed at the Fighting Against Cancer Medical Center (CLCC), Sétif, Algeria. The test was intended to verify physical compatibility between the custom fixation mechanism and the clinical treatment support system and to assess qualitative stability under manual pulling.

3. Results

3.1. Generation of the patient-specific model and final device design

The structured-light scanning workflow successfully generated a high-density patient facial mesh suitable for the immobilization system design. After sharpening and smoothing, the model preserved major facial landmarks while removing irregularities that could compromise fit. The resulting mesh served as a stable geometric basis for shell generation (Figure 2).

Figure 2. Patient-specific facial 3D model used for the immobilization system design obtained using structured-light scanning

The design workflow then produced a complete immobilization system composed of a personalized facemask, bilateral fixation belts, and attachment hooks. The final CAD assembly is shown in Figure 3, where the facial shell is anatomically driven, and the fixation components are board-driven. This dual-logic design proved advantageous because it separated patient-specific morphology from support-system mechanics.

The finalized STL geometry was sliced and printed successfully, resulting in a full immobilization device integrating facial conformity and clinical fixation capability (Figure 4). The fabrication/workflow time for the specific studied case of the cranial immobilization system is about one day. This parameter can be optimized for effective and wide clinical implementation if more sophisticated equipment is used. An optimization strategy is proposed in Section 4.

3.2. Thermal phase-transition behavior of polylactic acid and thermoplastic polyurethane

The phase-transition simulations demonstrated predictable melting behavior for both PLA and TPU. In PLA, temperature increased progressively, and the material transitioned smoothly from solid to molten, supporting a practical extrusion temperature of approximately 473 K (Figure 5A). TPU exhibited a similar overall transition pattern but heated and softened more rapidly, consistent with a practical extrusion temperature of approximately 493K (Figure 5B).

The main distinction between the two materials was the speed of thermal response. TPU absorbed and redistributed heat more rapidly than PLA, suggesting a narrower thermal control window during printing. PLA, by contrast, displayed a slower and more gradual heating profile. From a fabrication perspective, both materials were suitable for FDM, but TPU appeared more thermally responsive and therefore more sensitive to process settings.

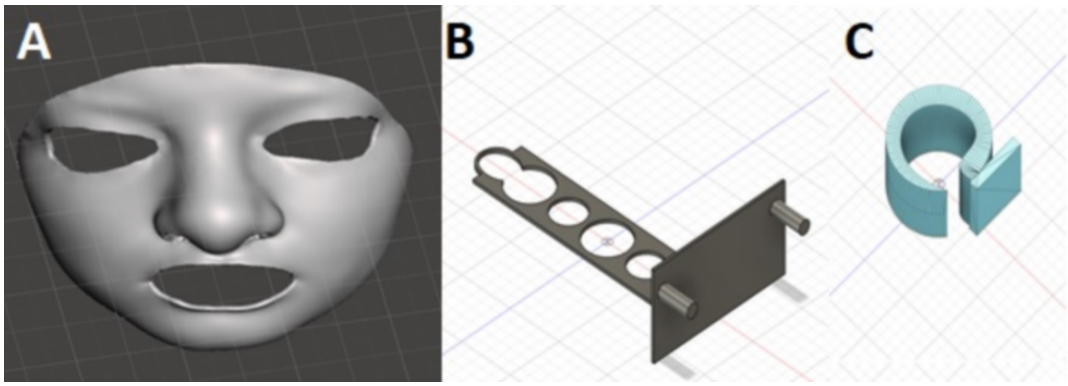

Figure 3. Computer-aided design of the personalized immobilization device: (A) patient-specific facemask generated in Meshmixer; (B) fixation belts designed in Fusion 360; (C) attachment hooks

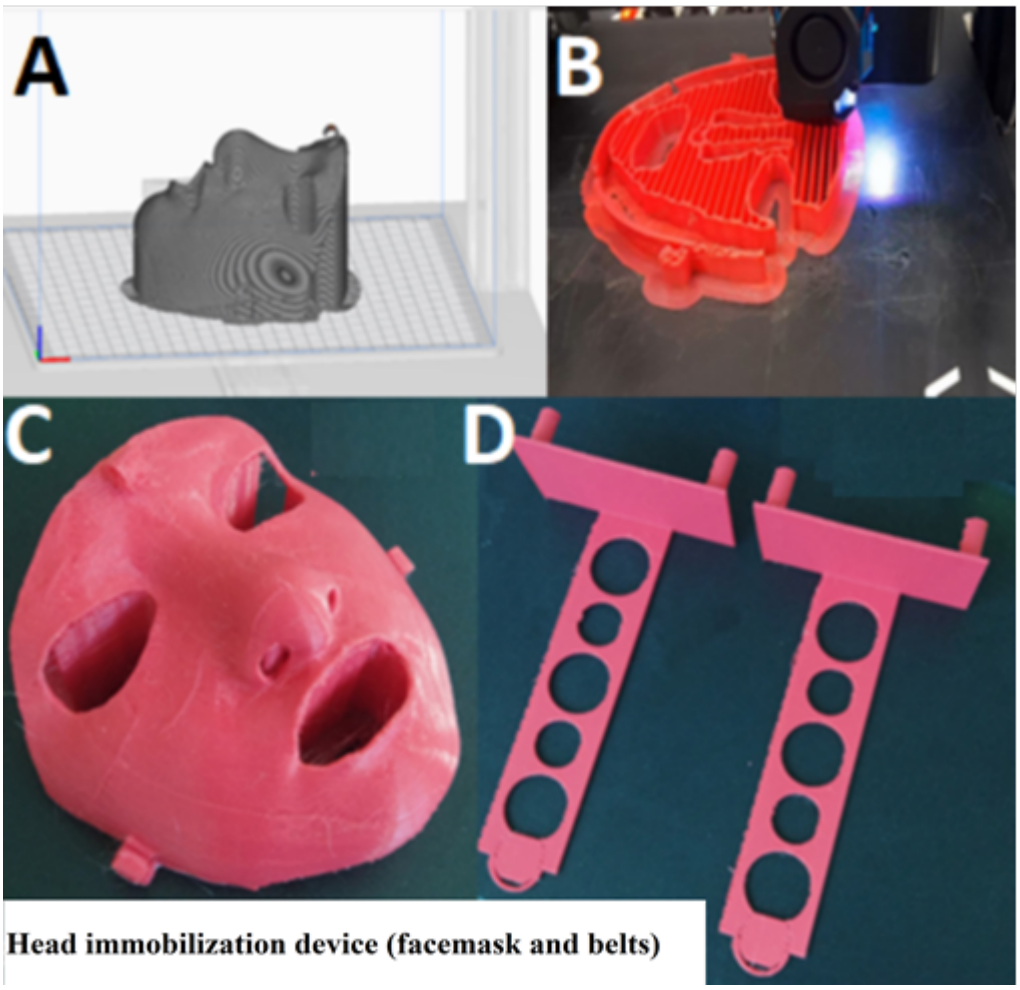

Figure 4. Slicing and 3D printing of the immobilization system. (A) Cura slicing interface. (B) Facemask under 3D printing. (C & D) Photographs of the (C) facemask and (D) belts.

3.3. Photon irradiation–induced heating

Under the simulated 6 MV irradiation conditions, both materials exhibited only minimal heating. The maximum temperature reached by PLA was 300.85 K, whereas TPU reached 301.45 K (Figure 6).

These temperatures are well below the critical thresholds associated with structural softening or deformation. For PLA, the measured thermal response remained well below its glass-transition temperature range of 328 K to 338 K, indicating that the material remained rigid during treatment. TPU, although intrinsically more flexible at room temperature, also remained thermally stable and showed no evidence of treatment-induced temperature elevation sufficient to threaten geometric integrity.

Taken together, these findings indicate that heat deposition from photon irradiation is unlikely to compromise the dimensional stability of either material under the studied treatment conditions.

3.4. Mechanical behavior of the fixation belts

3.4.1. Stress distribution

Mechanical simulations showed that the highest stress was not distributed uniformly along the fixation belts but was instead localized in the locking hinge region, the main load-transfer interface. This pattern was observed for both PLA and TPU (Figure 7A and 7C).

For both materials, the peak von Mises stress was approximately 0.7 MPa, far below the expected tensile strength range of the polymers. These results indicate a wide mechanical safety margin and argue against the risk of belt fracture or structural failure under the modeled traction conditions.

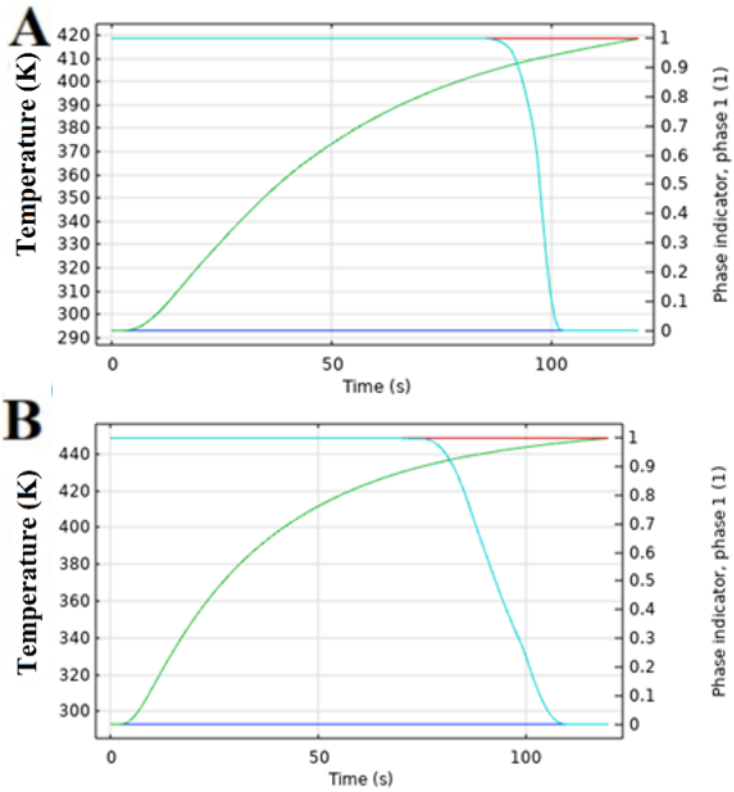

Figure 5. Thermal phase-transition simulation of the printing materials: (A) polylactic acid; (B) thermoplastic polyurethane

3.4.2. Displacement or deformation

The displacement analysis highlighted the clearest difference between PLA and TPU. The maximum displacement was 0.012 mm for PLA and 0.4 mm for TPU.

The PLA belt behaved as a nearly rigid component with negligible deformation (Figure 7B). TPU showed greater elastic deflection, as expected for a flexible elastomer, but its maximum displacement remained well below the 1-mm clinical tolerance threshold; this conservative submillimetric design criterion was adopted in this study for the belt deformation (Figure 7D).

From a clinical perspective, the most important point is not that TPU deformed more than PLA, but that the deformation remained submillimetric and therefore compatible with high-precision immobilization requirements. Indeed, the fitting test demonstrated that the fabricated fixation geometry physically matched the treatment table/indexing configuration and remained stable under manual traction.

3.5. Real clinical fitting test

The printed immobilization system was tested on the clinical treatment support system at CLCC Sétif. The tested system was designed for a healthy volunteer and tested in clinical conditions without beam (Figure 8). The immobilization system integrated correctly with the treatment table (couch) and indexing configuration, and once locked in place, it remained stable under manual traction (Figure 8). No looseness, detachment, or unstable motion was observed during the fitting test. Although this test did not constitute a full fractionated clinical validation study, it provided practical confirmation that the fixation concept was not merely digitally plausible but also physically compatible with the treatment environment.

The overall workflow outputs and the principal quantitative performance metrics of the fabricated immobilization system are summarized in Table 2. These include the mesh resolution from structured-light acquisition, the nominal mask thickness, the printing temperatures supported by phase-transition simulations, the maximum temperatures reached under photon irradiation, and the peak displacement and stress values from the mechanical analysis.

Finally, based on the obtained results, a benchmark of PLA and TPU for targeted application is presented in

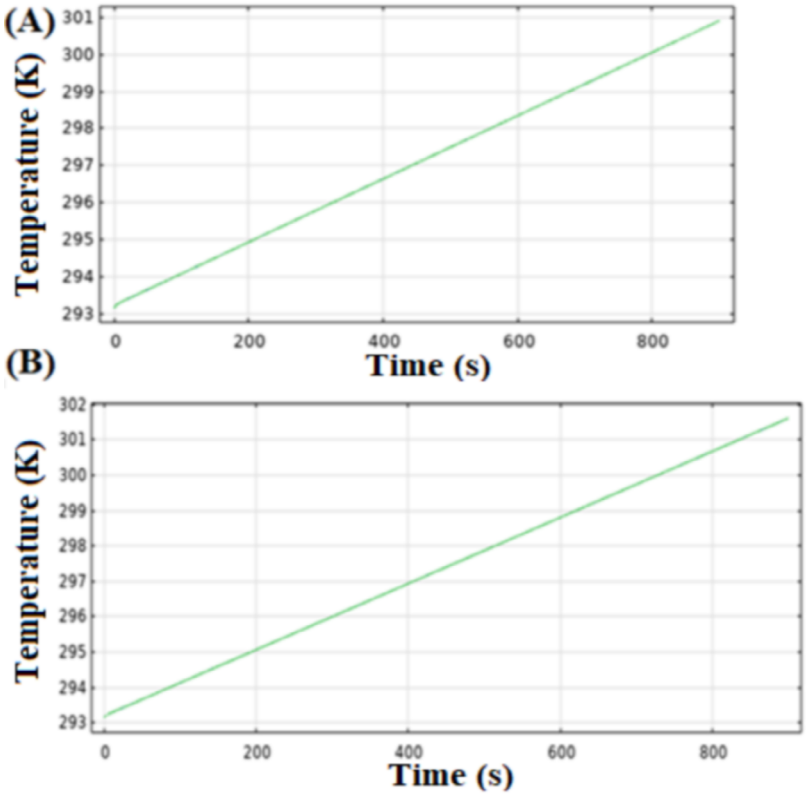

Figure 6. Simulation of photon irradiation–induced heating under a 6 MV photon beam. Evolution of mask temperature for (A) polylactic acid and (B) thermoplastic polyurethane over the simulated 15-min irradiation period

Table 2. Summary of workflow outputs and principal performance results

Domain	Parameter/Outcome	PLA	TPU
Device design	Nominal facemask thickness	2.5 mm design basis	2.5 mm design basis
Surface acquisition	Patient facial mesh	>4.9 million triangles	>4.9 million triangles
Printing behavior	Suggested print temperature from phase-transition simulation	~473 K	~493 K
Photon irradiation–induced heating	Maximum temperature under 6 MV, 400 MU/min for 15 min	300.85 K	301.45 K
Mechanical stress	Peak von Mises stress at locking region	~0.7 MPa	~0.7 MPa
Mechanical displacement	Maximum displacement	0.012 mm	0.4 mm
Clinical interpretation	Compliance with <1 mm setup tolerance	Yes	Yes
Practical fitting	Compatibility with treatment support system	Numerical reference only	Successful real fitting test

Abbreviations: PLA: Polylactic acid; TPU: Thermoplastic polyurethane.

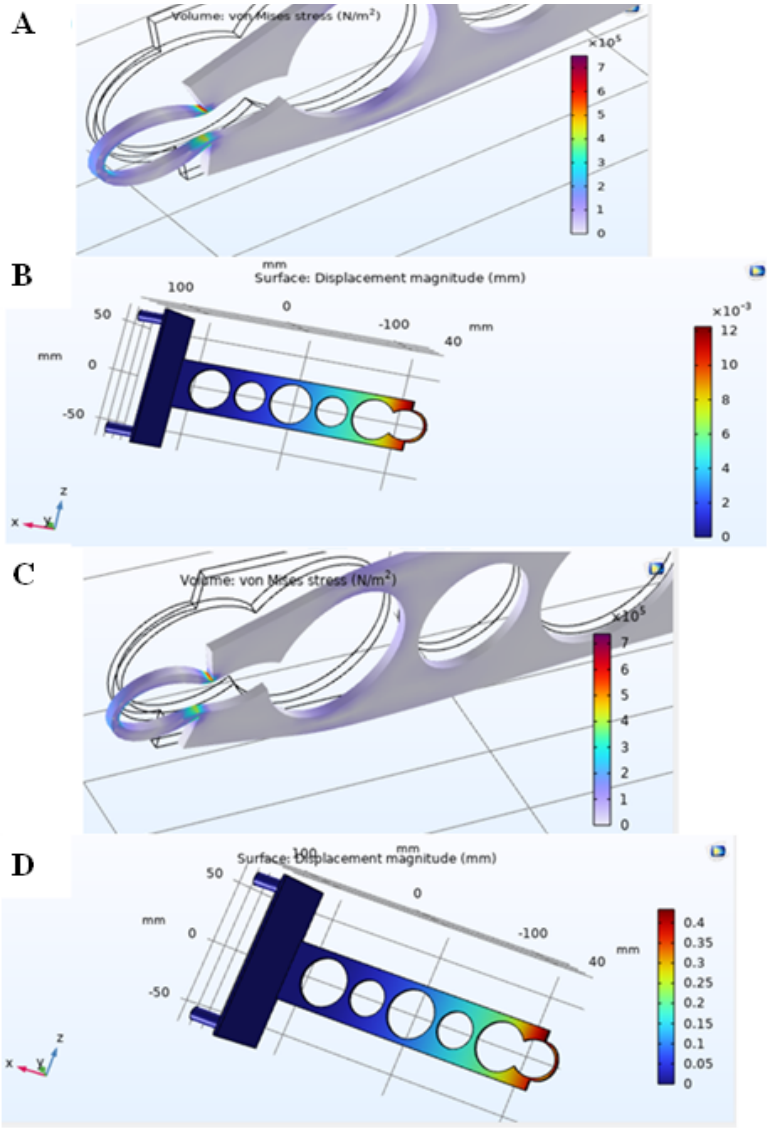

Figure 7. Mechanical simulation of fixation belts under clinical load. (A) von Mises stress distribution for polylactic acid (PLA). (B) Displacement map for PLA. (C) von Mises stress distribution for thermoplastic polyurethane (TPU). (D) Displacement map for TPU.

Table 3. Mechanically, both materials exhibited a peak simulated von Mises stress of approximately 0.7 MPa, compared with lower-bound tensile-strength values of approximately 50 MPa for PLA and 25 MPa for TPU used in the present material-property dataset. Thus, the simulated stress corresponds to only 1.4% and 2.8% of these conservative strength values, respectively. The maximum simulated displacement was 0.012 mm for PLA and 0.40 mm for TPU, both below the 1-mm submillimetric recommended deformation criterion adopted for the belt design. Thermally, the maximum temperatures during the simulated 6-MV, 400-MU/min, 15-min irradiation were 300.85 K (27.70 °C) for PLA and 301.45 K (28.30 °C) for TPU. For PLA, this is approximately 27 °C below the lower end of the 55 °C–65 °C glass-transition range used in the model. TPU should be interpreted differently because it is intentionally an elastomeric material at room temperature; its suitability is associated with its compliant mechanical behavior, adequate tensile strength, and the absence of clinically relevant irradiation-induced heating in the present simulation. Accordingly, the simulations support PLA as the more rigid option and TPU as the more compliant/comfort-oriented option.

Figure 8. Clinical fitting test of the 3D-printed immobilization device. Photograph of the printed device mounted on the Klarity Optek™ board/treatment support system during the practical test at Fighting Against Cancer Medical Center of Sétif.

Table 3. Mechanical and thermal benchmark of PLA and TPU for the 3D-printed head immobilization device

Criterion	PLA	TPU	Interpretation
Simulated peak von Mises stress (MPa)	~0.7	~0.7	Low applied stress
Conservative tensile-strength value used for screening (MPa)	50	25	Manuscript lower-bound values
Stress/strength ratio (%)	1.4	2.8	Large strength margin
Maximum simulated displacement (mm)	0.012	0.40	Both submillimetric
Study deformation criterion (mm)	1	1	Both satisfy criterion
Maximum irradiation temperature (K)	300.85	301.45	Very limited treatment heating
Glass-transition temperature (Tg; K)	328–338	233–253	Irradiation temperature far below PLA Tg; TPU remains in its flexible regime
Main advantage	High stiffness	Flexibility/Comfort	Different clinical roles

Abbreviations: PLA: Polylactic acid; TPU: Thermoplastic polyurethane.

4. Discussion

4.1. A practical workflow for personalized cranial immobilization

This study was designed around a pragmatic question rather than a purely conceptual one: can a personalized cranial immobilization device be created through a realistic digital workflow and still meet the mechanical and thermal expectations of radiotherapy? The answer, based on the present results, appears to be yes.

The principal strength of the work lies in the continuity of the workflow. The device was not designed as an isolated CAD object; it was developed through a chain that started with patient surface acquisition, passed through mesh cleaning and engineering design, and ended with fabrication, simulation, and real fitting. That matters because many promising 3D-printed concepts fail not because the printed object is impossible, but because the route from patient geometry to clinic-compatible hardware is poorly integrated. Here, the workflow remained coherent across all stages.[25-39]

Structured-light scanning played a key role in this chain. Unlike conventional thermoplastic mask molding, the acquisition step was non-contact and free of ionizing radiation. It transferred the burden of personalization from the patient's face to the digital environment. Instead of heating a thermoplastic sheet and shaping it directly over the patient, the present workflow first captured anatomy and then built the immobilization device around it. That distinction is clinically meaningful because it may reduce stress, claustrophobia, and discomfort, especially in patients who are already vulnerable or anxious.

4.2. Why the dual-design strategy worked

A second strength of the study is separating the facial shell from the fixation subsystem. The mask itself was anatomy-dependent and therefore appropriately handled in a mesh environment, whereas the belts and hooks were dimension-dependent and therefore better suited to parametric CAD. This may look like a simple software choice, but it reflects a deeper engineering logic. Immobilization devices have two obligations: they must fit the patient, and they must fit the treatment platform. Treating these as separate but connected design problems made the system easier to control and potentially easier to adapt in the future to other boards or head support systems.

4.3. Material behavior: rigidity versus comfort

The simulations suggest that both PLA and TPU are mechanically and thermally viable candidates for this application, but they do not serve the same clinical role.

Polylactic acid behaved as expected from a rigid polymer. It showed negligible displacement (0.012 mm), remained thermally stable during simulated photon irradiation, and would potentially maximize fixation stiffness. If pure rigidity were the only criterion, PLA would be an obvious candidate. However, immobilization is not only a structural problem; it is also a human–interface problem. A cranial mask must be worn repeatedly, often for several fractions, and a device that is perfectly rigid but poorly tolerated may not be the most practical solution.

Thermoplastic polyurethane occupies a more interesting position. Mechanically, it remained safely below the 1-mm tolerance threshold, with a maximum displacement of 0.4 mm. Thermally, it also remained stable under photon irradiation. At the same time, TPU offers a softer patient-contact interface and greater flexibility around the facial contours. That combination makes it particularly attractive for personalized immobilization, where comfort and conformity matter alongside rigidity. The present work therefore supports TPU not because it is the stiffest option, but because it appears to offer the best compromise between stability and wearability.

4.4. Thermal stability during treatment

One recurring concern with polymer-based radiotherapy accessories is whether photon irradiation could induce enough heating to deform the device or cause patient discomfort. The answer in this study was reassuring. Both materials remained close to room temperature under the simulated 6 MV beam conditions, with maximum temperatures below 30 °C. These values are far from the thermal thresholds associated with PLA softening or clinically relevant TPU deformation.

This is an important point for clinical translation. If the mask were to warm substantially during treatment, even a mechanically strong device could become unreliable. The present results suggest that, under the studied exposure conditions, treatment-induced heating is not a limiting factor.

4.5. Clinical meaning of the mechanical findings

The mechanical results deserve emphasis because they relate directly to radiotherapy precision. In high-precision cranial radiotherapy, submillimetric setup reproducibility is often the goal, especially when dose gradients are steep. In that context, the measured displacements, 0.012 mm for PLA and 0.4 mm for TPU, are clinically favorable. Both materials remained within a safe positional envelope, and stress concentration at the locking hinge remained far below material failure thresholds.

The locking hinge region emerged as the critical structural zone in both materials. This is mechanically plausible because it is where load transfer and constraint are concentrated. From a design standpoint, that observation is useful: future iterations of the device can focus reinforcement or topology optimization efforts on the hinge/lock geometry without unnecessarily thickening the entire structure.

4.6. Clinical value and current limitations

The present study demonstrates feasibility, mechanical plausibility, and thermal safety, but it is not yet a full clinical effectiveness study. Several limitations should be acknowledged. First, the work relied on preclinical simulation and practical fitting, not on a prospective clinical series with daily image-guided verification. As a result, although the device appears stable, the present study does not quantify inter-fraction setup errors, rotational reproducibility, or patient-specific residual motion under real treatment conditions. Second, while both PLA and TPU were characterized numerically, the fabricated prototype was centered mainly on TPU, which means that direct head-to-head physical comparison of printed PLA versus printed TPU masks was not performed in routine clinical use. Third, the fitting test demonstrated compatibility with the treatment table and locking system, but it did not yet address long-term operational questions such as cleaning/disinfection durability, repeated use over multiple fractions, or workflow time in a busy department.

Fourth, the study focused on the mechanical and thermal response of the immobilization device rather than its dosimetric effect. Although the carbon-fiber indexing board and the polymer mask are expected to have limited influence compared with denser materials, a dedicated dosimetric analysis of attenuation and build-up effects would strengthen future work.

These limitations do not reduce the value of the present study; rather, they define the next steps. The device has now crossed the threshold from concept to preclinical feasibility. The logical continuation is a prospective clinical validation study combining setup imaging, patient-reported comfort, fabrication time, and dosimetric verification.

4.7. Optimization pathway

The current workflow contains surface acquisition → mesh processing → shell design → belt/hook CAD → STL export → slicing → FDM printing → post-processing → fitting. The largest opportunities for acceleration are:

- Faster high-resolution optical scanner with automated registration,
- Validated automated mesh-cleaning pipeline,
- Parametric/automated CAD template,
- Library of validated parametric designs,
- Validated material-specific profile,
- Higher-throughput/multi-nozzle or industrial FDM system.

A faster workflow is not necessarily a better clinical workflow. For clinical translation, we recommend defining a multidimensional optimization criterion:

$$J = w_1 T_{fabrication} + w_2 E_{geometric} + w_3 u_{max} + w_4 T\sigma_{vM,max} + w_5 C_{material} + w_5 C_{p} \quad (17)$$

where $T_{fabrication}$ is the total turnaround time, $E_{geometric}$ is the scan/CAD/printed-part dimensional error, u_{max} is the maximum belt displacement, $\sigma_{vM,max}$ is the maximum stress, $C_{material}$ is the material/process cost, $C_{patient}$ is the patient-comfort penalty, and w_i is the clinically selected weighting factor.

This proposed route supports multi-objective optimization. Indeed, published clinical studies show that immobilization accuracy is affected by the design and preparation of immobilization systems. For example, in their prospective study of 29 patients and 528 setup errors, Contesini *et al.*[40] found that aspects of customized immobilization preparation influenced setup error.

5. Conclusion

This study developed and characterized a patient-specific cranial immobilization device for radiotherapy using a digital workflow that integrated structured-light facial acquisition, mesh post-processing, dual CAD design, FDM 3D printing, and multiphysics validation. The workflow successfully fabricated a personalized 2.5-mm-thick facial mask with lateral fixation components compatible with a clinical indexing board. COMSOL Multiphysics simulations showed that both PLA and TPU remained thermally stable during simulated 6 MV photon irradiation and mechanically reliable under clinical loading. PLA offered near-rigid behavior with minimal displacement, whereas TPU combined acceptable submillimetric deformation with a more compliant patient-contact profile. The fabricated device also demonstrated successful table integration and stable locking during real clinical fitting tests.

Overall, the study supports the feasibility of 3D-printed personalized cranial immobilization as a credible alternative to conventional thermoplastic masks. More importantly, it provides a reproducible workflow, from surface acquisition to physical fitting, that can serve as a platform for future clinical translation. The next stage

should involve prospective patient evaluation with setup reproducibility metrics, comfort scoring, and dosimetric assessment in routine radiotherapy practice.

Acknowledgments

None.

Funding

None.

Conflict of interest

The authors declare they have no competing interests.

Author contributions

Conceptualization: Faycal Kharfi
Formal analysis: All authors
Investigation: All authors
Methodology: Faycal Kharfi
Writing–original draft: NourElHouda Touil, Faycal Kharfi
Writing–review & editing: Faycal Kharfi

Ethics approval and consent to participate

Not applicable. The practical fitting tests of the developed product were performed on a volunteer (first author: NourElHouda Touil) in clinical positioning conditions and without any irradiation.

Consent for publication

Not applicable.

Availability of data

Data are available from the corresponding author upon reasonable request.

References

1. Khan FM. *The Physics of Radiation Therapy*. 3rd ed. Philadelphia: Lippincott Williams & Wilkins; 2003.
2. Delaney G, Jacob S, Featherstone C, Barton M. The role of radiotherapy in cancer treatment. *Cancer*. 2005;104(6):1129-1137.

   doi: 10.1002/cncr.21324
3. Baskar R, Lee KA, Yeo R, Yeoh KW. Cancer and radiation therapy: current advances and future directions. *Int J Med Sci*. 2012;9(3):193-199.

   doi: 10.7150/ijms.3635
4. Verellen D, De Ridder M, Linthout N, Tournel K, Soete G, Storme G. Innovations in image-guided radiotherapy. *Nat Rev Cancer*. 2007;7(12):949-960.

   doi: 10.1038/nrc2288
5. Mackie TR, Kapatoes J, Ruchala K, *et al.* Image guidance for precise conformal radiotherapy. *Int J Radiat Oncol Biol Phys*. 2003;56:89-105.

   doi: 10.1016/s0360-3016(03)00090-7
6. Rosenthal DI, Chambers MS, Fuller CD, *et al.* Beam path toxicities to non-target structures during intensity-modulated radiation therapy for head and neck cancer. *Int J Radiat Oncol Biol Phys*. 2008;72(3):747-755.

   doi: 10.1016/j.ijrobp.2008.01.012
7. Tryggestad E, Christian M, Ford E, *et al.* Inter- and intrafraction patient positioning uncertainties for intracranial radiotherapy: a study of four frameless, thermoplastic mask-based immobilization strategies using daily cone-beam CT. *Int J Radiat Oncol Biol Phys*. 2011;80(1):281-290.

   doi: 10.1016/j.ijrobp.2010.06.022
8. Li G, Ballangrud A, Kuo LC, *et al.* Motion monitoring for cranial frameless stereotactic radiosurgery using video-based three-dimensional optical surface imaging. *Med Phys*. 2011;38(7):3981-3994.

   doi: 10.1118/1.3596526
9. Onimaru R, Shirato H, Fujino M, *et al.* The effect of tumor location and respiratory function on tumor movement estimated by real-time tracking radiotherapy (RTRT) system. *Int J Radiat Oncol Biol Phys*. 2005;63(1):164-169.

   doi: 10.1016/j.ijrobp.2005.01.025
10. Cerviño LI, Gupta S, Rose MA, Yashar C, Jiang SB. Using surface imaging and visual coaching to improve the reproducibility and stability of deep-inspiration breath hold for left-breast-cancer radiotherapy. *Phys Med Biol*. 2009;54(22):6853-6865.

    doi: 10.1088/0031-9155/54/22/007
11. Rengier F, Mehndiratta A, von Tengg-Kobligk H, *et al.* 3D printing based on imaging data: review of medical applications. *Int J Comput Assist Radiol Surg*. 2010;5(4):335-341.

    doi: 10.1007/s11548-010-0476-x
12. Mitsouras D, Liacouras P, Imanzadeh A, *et al.* Medical 3D Printing for the Radiologist. *Radiographics*. 2015;35(7):1965-1988.

    doi: 10.1148/rg.2015140320
13. Martelli N, Serrano C, van den Brink H, *et al.* Advantages and disadvantages of 3-dimensional printing in surgery: A systematic review. *Surgery*. 2016;159(6):1485-1500.

    doi: 10.1016/j.surg.2015.12.017
14. Fredieu JR, Kerbo J, Herron M, Klatte R, Cooke M. Anatomical models: a digital revolution. *Med Sci Educ*. 2015;25(2):183-194.

doi: 10.1007/s40670-015-0115-9

15. Canters RA, Lips IM, Wendling M, *et al.* Clinical implementation of 3D printing in the construction of patient specific bolus for electron beam radiotherapy for non-melanoma skin cancer. *Radiother Oncol*. 2016;121(1):148-153.

    doi: 10.1016/j.radonc.2016.07.011

16. Burleson S, Baker J, Hsia AT, Xu Z. Use of 3D printers to create a patient-specific 3D bolus for external beam therapy. *J Appl Clin Med Phys*. 2015;16(3):166-178.

    doi: 10.1120/jacmp.v16i3.5247

17. Rooney MK, Rosenberg DM, Braunstein S, *et al.* Three-dimensional printing in radiation oncology: A systematic review of the literature. *J Appl Clin Med Phys*. 2020;21(8):15-26.

    doi: 10.1002/acm2.12907

18. Katamesh AA, Subaiea GM, Mostafa M, *et al.* Revolutionizing Cancer Care: The Role of 3D Printing in Personalized Oncology. *ACS Omega*. 2025;10(35):39350-39370.

    doi: 10.1021/acsomega.5c01642

19. Bell T, Li B, Zhang S. Structured Light Techniques and Applications. In: Webster JG, ed. *Wiley Encyclopedia of Electrical and Electronics Engineering*. Hoboken, New Jersey: Wiley; 2016.

    doi: 10.1002/047134608x.w8298

20. Geng J. Structured-light 3D surface imaging: a tutorial. *Adv Opt Photonics*. 2011;3(2):128-160.

    doi: 10.1364/AOP.3.000128

21. Sansoni G, Trebeschi M, Docchio F. State-of-the-art and applications of 3D imaging sensors in industry, cultural heritage, medicine, and criminal investigation. *Sensors*. 2009;9(1):568-601.

    doi: 10.3390/s90100568

22. Kharfi F, Belatar M, Benkahila K. 3D-printed personalized bolus designed through structured-light scanning for adaptive radiotherapy. *Adv Radiother Nucl Med.* 2025;3(4):38-48.

    doi: 10.36922/ARNM025250032

23. Dhawan AP, D'Alessandro B, Fu X. Optical imaging modalities for biomedical applications. *IEEE Rev Biomed Eng*. 2010;3:69-92.

    doi: 10.1109/RBME.2010.2081975

24. Baumann FW, Schuermann M, Odefey U, Pfeil M. From G-code to STL: reconstruct models from 3D printing as a service. In: *IOP Conference Series: Materials Science and Engineering*. Bristol: IOP Publishing; 2017;280(1):012033.

    doi: 10.1088/1757-899X/280/1/012033

25. Chia HN, Wu BM. Recent advances in 3D printing of biomaterials. *J Biol Eng*. 2015;9:4.

    doi: 10.1186/s13036-015-0001-4

26. Ventola CL. Medical applications for 3D printing: current and projected uses. *Pharm Ther.* 2014;39(10):704-711.

27. Javaid M, Haleem A. Current status and challenges of Additive manufacturing in orthopaedics: An overview. *J Clin Orthop Trauma*. 2019;10(2):380-386.

    doi: 10.1016/j.jcot.2018.05.008

28. Tack P, Victor J, Gemmel P, Annemans L. 3D-printing techniques in a medical setting: a systematic literature review. *Biomed Eng Online*. 2016;15(1):115.

    doi: 10.1186/s12938-016-0236-4

29. Salmi M. Additive manufacturing processes in medical applications. *Materials*. 2021;14(1):191.

    doi: 10.3390/ma14010191

30. Rankin TM, Giovinco NA, Cucher DJ, Watts G, Hurwitz B, Armstrong DG. Three-dimensional printing surgical instruments: are we there yet? *J Surg Res*. 2014;189(2):193-197.

    doi: 10.1016/j.jss.2014.02.020

31. Schubert C, van Langeveld MC, Donoso LA. Innovations in 3D printing: a 3D overview from optics to organs. *Br J Ophthalmol*. 2014;98(2):159-161.

    doi: 10.1136/bjophthalmol-2013-304446

32. Melchels FPW, Domingos MAN, Klein TJ, Malda J, Bartolo PJ, Hutmacher DW. Additive manufacturing of tissues and organs. *Prog Polym Sci*. 2012;37(8):1079-1104.

    doi: 10.1016/j.progpolymsci.2011.11.007

33. Gross BC, Erkal JL, Lockwood SY, Chen C, Spence DM. Evaluation of 3D printing and its potential impact on biotechnology and the chemical sciences. *Anal Chem*. 2014;86(7):3240-3253.

    doi: 10.1021/ac403397r

34. Javaid M, Haleem A, Vaishya R, Bahl S, Suman R, Vaish A. Industry 4.0 technologies and their applications in fighting COVID-19 pandemic. *Diabetes Metab Syndr*. 2020;14(4):419-422.

    doi: 10.1016/j.dsx.2020.04.032

35. Direkwatana C, Rattanapan N. 3D printing process for patient-specific models and applications. *Rama Med J*. 2025;48(2):e270830.

    doi: 10.33165/rmj.48.02.e270830

36. Salmi M, Tuomi J, Paloheimo K, *et al.* Patient-specific reconstruction with 3D modeling and DMLS additive manufacturing. *Rapid Prototyp J.* 2012;18(3):209-214.

    doi: 10.1108/13552541211218126

37. Rybicki FJ. Medical 3D printing and the physician-artist.

Lancet. 2018;391(10121):651-652.

doi: 10.1016/S0140-6736(18)30212-5

38. Kharfi F, Benkahila K, Boulkhessaim F, *et al*. Implementation of 3D Printing and Modeling Technologies for the Fabrication of Dose Boluses for External Radiotherapy at the CLCC of Sétif, Algeria. *Technol Cancer Res Treat*. 2024;23.

    doi: 10.1177/15330338241266479

39. Ghediri N, Kharfi F, Benkahila K, *et al*. Dosimetric Validation and Surface Fit Evaluation of 3D-Printed Dose Boluses for Radiation Therapy Applications. *Int J Cancer Manag*. 2025;18(1):e159515.

    doi: 10.5812/ijcm-159515

40. Contesini M, Guberti M, Saccani R, *et al*. Setup errors in patients with head-neck cancer (HNC), treated using the Intensity Modulated Radiation Therapy (IMRT) technique: how it influences the customised immobilisation systems, patient's pain and anxiety. *Radiat Oncol*. 2017;12(1):72.

    doi: 10.1186/s13014-017-0807-y